ELSEVIER

Journal of Molecular Catalysis A: Chemical 106 (1996) 125–134

JOURNAL OF MOLECULAR CATALYSIS A: CHEMICAL

Characterization of nickel species on several γ-alumina supported nickel samples

P. Salagre [a], J.L.G. Fierro [b], F. Medina [c], J.E. Sueiras [c,*]

[a] *Dpt. de Química, Facultat de Química, Universitat Rovira i Virgili, Pl. Imperial Tarraco, 1.43005 Tarragona, Spain*
[b] *Instituto de Catálisis y Petroleoquímica, C.S.I.C., Campus UAM, Cantoblanco, 28049 Madrid, Spain*
[c] *Dpt. d'Enginyeria Química, ETSE, Universitat Rovira i Virgili, Pl. Imperial Tarraco, 1.43005 Tarragona, Spain*

Received 12 May 1995; accepted 23 August 1995

Abstract

Studies of the chemical preparation, surface areas, pore distributions, powder X-ray diffraction (XRD), scanning electron microscopy (SEM) and X-ray photoelectron spectra (XPS) of several γ-alumina supported nickel samples active for the catalytic hydrogenation of hexanedinitrile have been carried out. NiO crystallites showed to be larger than the pore mouths of the support. Pore distributions lie in the mesopore region with diameters between 20 and 100 Å. Powder XRD detects the oxidized and reduced-nickel phases present and does not detect the nickel aluminate phase, due to the lack of crystallinity of the latter. SEM micrographs detect the presence of octahedral NiO crystallites and amorphous shelling nickel aluminate. XPS results show the presence of surface Ni^{2+} (in the form of stoichiometric and non-stoichiometric NiO, and stoichiometric and non-stoichiometric nickel aluminates) and surface reduced nickel. A deconvolution of the experimental curves was carried out in order to obtain a better assignment of the surface nickel species present. Nickel aluminate is detected at calcination temperatures > 623 K and covers all the surface of the support with layers between zero and several atoms thick, depending on calcination temperature and nickel concentration. Catalytically active reduced nickel (for nitrile hydrogenations) either as naked crystallites or as encapsulated nickel inside voided non-stoichiometric aluminate shells lie on top of the underlying catalytically inactive nickel aluminate when precursor calcination temperatures are higher than 623 K and reduction temperatures of 673 K. NiO transformation into nickel aluminate collapses the cubic NiO surface morphology of the small NiO crystallites giving rise to voided shells of nickel aluminate which may hide encapsulated reducible NiO.

Keywords: Nickel; Alumina; Hydrogenation; Hexanedinitrile; Supported catalysts

1. Introduction

The hydrogenation of nitriles is probably the most widely employed method of commercially produced amines. The 1,6-hexanedinitrile (adiponitrile) is used as starting material to obtain 6-aminohexanenitrile and 1,6-hexanediamine [1]. The industrial preparation of the afore-mentioned primary amines is usually accomplished in the liquid phase at elevated hydrogen pressures (270–600 bar) and at 30 bar in some recent process, where the catalyst repre-

* Corresponding author. Tel.: (+34-77)559787; fax: (+34-77)559597.

SSDI 1381-1169(95)00256-1

sents a very important factor in determining the selectivity with respect to primary amines [2]. Recently, catalysts working at 1 atm hydrogen pressure based on free and potassium-doped nickel have been reported [3–6]. Secondary amines can be prepared in liquid phase with satisfactory selectivity using rhodium- or copper-based catalysts [7].

The surface characterization and activities of several γ-alumina supported nickel catalysts were reported in a previous article [8]. The hydrogenation of acetonitrile on γ-alumina supported nickel [9], the effect of γ-alumina on the surface properties of the catalyst [10–13] and the nickel/γ-alumina interaction [14–21] have been studied extensively. However, in our opinion, additional insight is needed in the structural characterization of the nickel species involved in γ-alumina supported nickel catalysts for the selective hydrogenation of adiponitrile, in a continuous process. Here, we report the preparation and structural characterization of several γ-alumina supported nickel solids with potential catalytic activity, for the afore-mentioned hydrogenation reaction at 1 atm pressure.

2. Experimental

2.1. Sample preparations

The NiO/γ-alumina was prepared by impregnation of γ-alumina (BET area, 205 m^2/g) with different amounts of aqueous nickel nitrate solutions to obtain the nickel contents shown in Table 1, followed by drying at 393 K and air calcinations at 623, 773 and 1023 K. Samples were reduced with hydrogen–argon mixtures for 20 hours, with a 1:20 volume ratio, an initial space velocity of 360 h^{-1} (with respect to hydrogen), and a temperature of 673 K. The resulting samples will be designated hereafter as samples 1–15, 1 and 9 being pure γ-alumina and pure NiO, respectively.

All reagents were reagent-grade (Aldrich) and pure gases were dried and deoxygenated.

2.2. Air-free sampling

The samples were always handled under air-free conditions, after the reduction step. The solids were transferred in degassed isooctane and under hydrogen atmosphere at room temperature. The isooctane surface-impregnated samples were further isolated from the air with sticky tape and mounted in a glove box for XRD monitoring. Alternatively, the isooctane-impregnated samples were vacuum pumped in the pre-evacuation chamber of the photoelectron spectrometer, not resulting in significant air oxidation by this procedure. Gas purges, positive gas pressures and Schlenk techniques were used when necessary.

2.3. BET surface areas and pore distributions

BET surface areas were calculated from the nitrogen adsorption isotherms at 77 K using a Micromeritics ASAP 2000 surface analyzer, and a value of 0.164 nm^2 for the cross-section of the nitrogen molecule. The same equipment calculates the pore distribution for diameters between 10 and 3000 Å using the method of Barrett, Joyner and Halenda (BJH) [22].

Table 1
Nickel loading and calcination temperatures of the nickel/γ-alumina samples

Sample	g Nickel/g γ-alumina	Calcination temp. (K)
1	Pure Al_2O_3	623
2	0.033	623
3	0.066	623
4	0.133	623
5	0.200	623
6	0.266	623
7	0.400	623
8	0.533	623
9	Pure NiO	623
10	0.066	773
11	0.266	773
12	0.533	773
13	0.066	1023
14	0.266	1023
15	0.533	1023

2.4. X-ray diffraction (XRD)

Powder X-ray diffraction (XRD) patterns of the samples were obtained with a Philips PW 1010 diffractometer using nickel-filtered Cu-K α radiation. Samples were dusted on double-sided sticky tape and mounted on glass microscope slides. The patterns were recorded for $5 \leqslant 2\theta/\text{degrees} \leqslant 85$ and crystalline phases were identified using the JCPDS files.

2.5. Scanning electron microscopy (SEM)

Scanning electron micrographs were obtained in a JEOL JSM-35C microscope operating at WD = 9 mm and magnification values of $\times$37000–43000. Micrographs were taken at voltages of 25–35 kV.

2.6. X-ray photoelectron spectroscopy

X-ray photoelectron spectra were recorded on a Leybold LHS 10 spectrometer provided with a hemispherical energy analyzer and a Mg-K α X-irradiation source. Powdered samples were pressed using small stainless-steel cylinders and mounted on a standard sample probe, placed in a pre-evacuation chamber up to ca. 10^{-5} Torr, before they were moved into the main vacuum chamber. The residual pressure in the turbo-pumped analysis chamber was kept below 7×10^{-9} Torr during data collection. Each spectral region was signal-averaged for a given number of scans to obtain good signal-to-noise ratios. Although surface charging was observed on all the samples, accurate binding energies (BE) were determined by charge referencing with the C 1s line at 284.9 eV. Peak areas of Ni(0) and Ni(II) including satellites, were computed by a program which assumed Gaussian line-shapes and flat background subtraction.

Table 2
Surface characterization of several nickel/γ-alumina catalyst precursors

Sample	BET area (m^2/g) [a]	Area contribution (m^2) based on pure γ-alumina [b]	Average pore diameter (Å) [c]
1	205	205	57
2	202	197	53
3	188	189	52
4	173	175	51
5	158	164	49
6	150	153	47
7	135	136	47
8	121	123	46

[a] BET area of pure NiO, 10 m^2/g.
[b] Area of the % pure γ-alumina content in precursor, calculated from the value of 205 m^2/g.
[c] Calculated from the method of Barrett, Joyner and Halenda [22].

3. Results and discussion

3.1. BET areas and pore distributions

Table 2 depicts the BET areas of the samples 1–8 calcined at 623 K. These values are not significantly different from those surface areas calculated on the basis of the sum of % pure γ-alumina and % NiO contents in precursors, using the value of 205 m^2/g as the BET area of pure γ-alumina. The decrease of the area observed on going from 2 to 8 is mainly due to the % weight decrease of γ-alumina (main contributor to the total area) composition indicating a low NiO dispersion or large NiO crystallites present. The very small change of pore diameters from samples 1 to 8, in Table 2, may be indicative of the presence of NiO crystallites larger than the pore mouths of the γ-alumina which prevent pores from blocking; consequently, the surface area is maintained with respect to the area of the pure γ-alumina of the sample composition. These results are in agreement with those obtained from other techniques as shown below. Also, Fig. 1 shows the nitrogen adsorption–desorption isotherms for pure γ-alumina (sample 1), the lower loaded Ni/γ-alumina (sample 2) and the higher loaded Ni/γ-alumina (sample 8). Fig. 2 shows the pore distributions, according to the BJH method, as the plot of $dV/d\log(D)$ desorption pore vol-

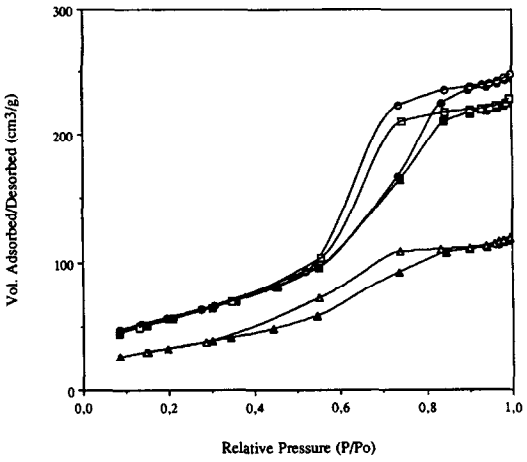

Fig. 1. Nitrogen adsorption (full symbols)/desorption (empty symbols) isotherms at 77 K for pure γ-alumina, sample 1 (●, ○), and the nickel loaded γ-alumina samples 2 (■, □) and 8 (▲, △).

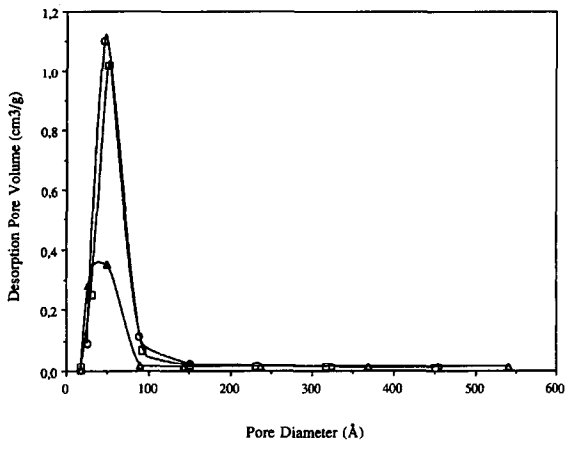

Fig. 2. Pore distribution plot for pure γ-alumina, sample 1 (○), and the nickel loaded γ-alumina samples 2 (□) and 8 (△).

ume vs. pore diameter for the same samples of Fig. 1, where V = pore volume (ml/g), D = pore diameter (Å). Two features may be extracted from these figures. First, all samples show isotherms of the type IV in the classification of Brunauer, Deming, Deming and Teller (BDDT) [23], then mesoporous solids having hysteresis loops of decreasing volume capacities

Table 3
XRD and XPS characterization of several nickel/γ-alumina samples [a]

Samples [b]	Crystal phases (XRD) [c]	E_b (eV) (XPS) of Ni $2p_{3/2}$ levels after curve deconvolution	Surface atomic ratio Ni/Al	Surface/chemical Ni/Al ratios
2	–	857.0	0.067	2.31
3	–	855.6; 857.3	0.100	1.72
6	NiO	855.3; 857.1	0.626	2.72
8	NiO	855.5; 857.3	0.907	1.96
9	NiO	855.0; 856.9	–	–
2r	–	852.9; 856.8	0.060	2.07
3r	–	852.6; 856.7	0.081	1.40
6r	Ni	852.6; 856.4	0.456	1.98
8r	Ni	852.7; 856.6	0.675	1.46
9r	Ni	852.7; 854.5	–	–
10	–	856.0; 857.0	0.053	0.91
11	NiO	855.6; 856.8	0.192	0.83
12	NiO	855.3; 856.8	1.481	3.20
10r	–	853.1; 856.8	0.049	0.84
11r	Ni	853.0; 855.5; 856.9	0.163	0.71
12r	Ni	852.9; 856.8	1.110	2.40
13	–	856.8	0.029	0.50
14	NiO	855.5; 856.8	0.281	1.22
15	NiO	855.5; 857.1	0.993	2.16
13r	–	856.9	0.028	0.48
14r	–	852.9; 856.0; 858.0	0.284	1.23
15r	Ni	852.7; 856.0; 858.0	0.754	1.64

[a] Except for samples 9 and 9r which are made of pure nickel and zero content of γ-alumina.
[b] r = sample reduced at 673 K after corresponding calcination as shown in Table 1.
[c] Other than γ-alumina.

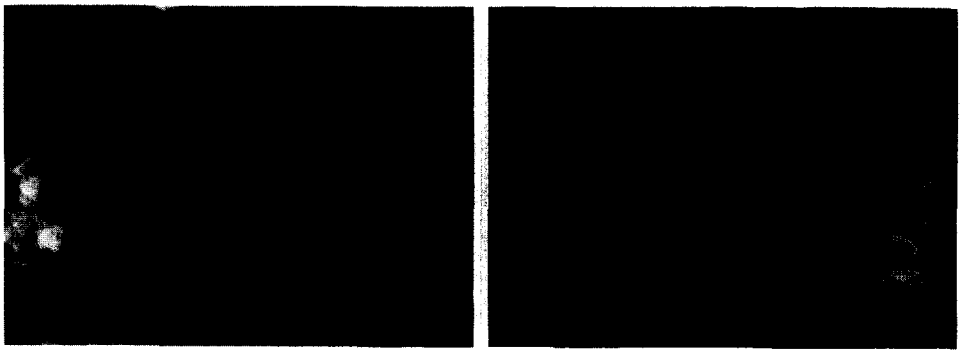

Fig. 3. Scanning electron micrographs taken from the surface of the high nickel loaded sample 7.

with decreasing alumina content (Table 2) [24]. Samples 1, 2 an 8 in Fig. 2 show similar pore distribution plots in the mesopore region and similar average pore diameters, 46–53 Å, the difference in total volume or number of pores being due to the fact that sample 2 contains 60% more γ-alumina than sample 8. Samples 3–7 exhibit pore distribution plots with shapes in between of those shown from samples 2 and 8, respectively. Secondly, the samples studied show the absence of pore diameters of 1000 Å, in the macropore region, exhibiting a flat baseline from 200 Å up to 1000 Å, at least, which means that NiO crystallites of sizes larger than 300 Å cannot penetrate and efficiently block the pore mouths of the support. Consequently, the great similarities obtained from the surface characterization of the samples 1–8 drive to the conclusion that NiO crystallites must be of sizes quite larger than 300 Å which should keep the surface areas and pore distributions of the support almost unchanged.

3.2. Powder X-ray diffraction

Table 3 depicts the crystalline phases detected by powder X-ray diffraction for the samples, prepared at different calcination temperatures and for different nickel contents, as described in the Experimental section. The NiO and Ni diffraction lines are usually weak in the nickel/γ-alumina system, owing mainly to the low crystallinity obtained from the NiO/γ-alumina interaction. The low intensity-NiO diffraction lines are observed only for those samples with the higher nickel content (> 0.266 g Ni/γ-alumina). The nickel aluminate spinel phase was not detected, probably due to the lack of crystallinity. The line intensities corresponding to the reduced nickel phases increased with nickel content paralleling the increase of crystallite size which is in the range of 1000–2000 Å, for samples 7 and 8, according to SEM micrographs.

3.3. Scanning electron microscopy (SEM)

Stereographic pictures of samples 7 and 5 taken from a scanning electron microscope are shown in Figs. 3 and 4, respectively. The highly nickel loaded sample 7 shows clearly differenti-

Fig. 4. Scanning electron micrograph taken from the surface of the mid nickel loaded sample 5.

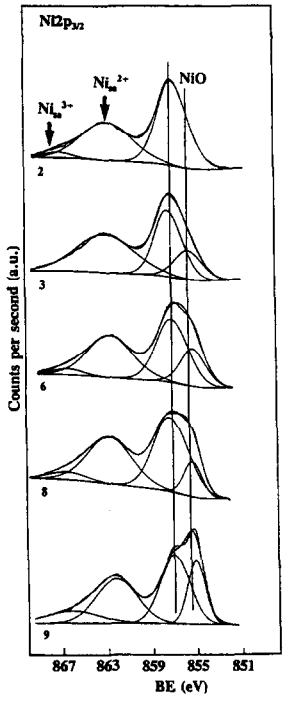

Fig. 5. XPS nickel/γ-alumina (oxidic samples 2–9 calcined at 623 K) for the Ni $2p_{3/2}$ level.

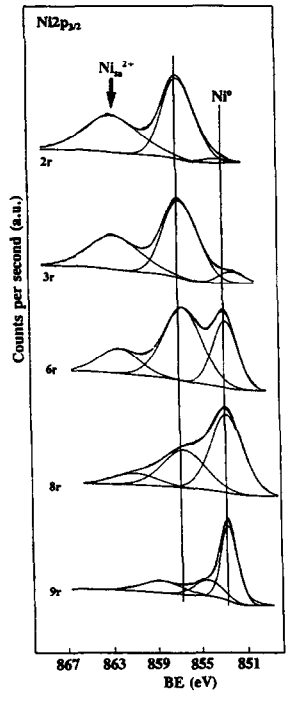

Fig. 6. XPS nickel/γ-alumina (samples 2r–9r reduced at 673 K, previously calcined at 623 K) for the Ni $2p_{3/2}$ level.

ated NiO octahedra of the same size, ca. 2000 Å, on the surface of the γ-alumina support. On the other hand, the less nickel loaded sample 5 shows the NiO octahedra encapsulated inside a porous shell. That shell has been recently interpreted as a non-stoichiometric phase of nickel aluminate [30,32,8]. We also found, in results to be published, that a third phase is found of a homogeneously distributed thin layer of stoichiometric nickel aluminate upon all the surface of the support, for nickel loadings of sample 3 and lower, where the metal–support interaction increases.

3.4. X-ray photoelectron spectroscopy

Table 3 lists the binding energies (E_b) corresponding to the Ni $2p_{3/2}$ level for some of the more representative samples. The values indicated in Table 3 and the included peaks shown in Figs. 4–7 arise from the deconvolution of the overall experimental peaks in their components,

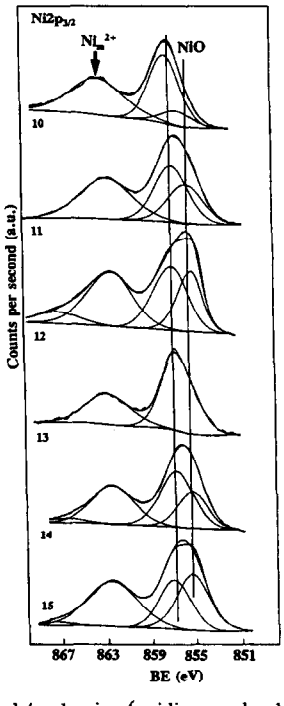

Fig. 7. XPS nickel/γ-alumina (oxidic samples 10–12 and 13–15 calcined at 773 and 1023 K, respectively) for the Ni $2p_{3/2}$ level.

calculated from a curve synthesis process in which a Gaussian/Laurentian mix of variable proportion was applied to obtain the recorded spectra (the two overall lines corresponding to the experimental and fitting curves). First of all, as shown in Table 3 and Fig. 5, unsupported nickel in the oxidic form as black non-stoichiometric NiO, sample 9, shows two characteristic primary peaks at $E_b = 855.0$ and 856.9 eV corresponding to Ni^{2+} and Ni^{3+}, respectively; the latter showing a higher binding energy, as expected (E_b of the metal increases when the covalency decreases) [15]. Also the presence of the NiO two satellites at 862.2 eV (stoichiometric green NiO) and 867 eV (non-stoichiometric black NiO) should be noted, the latter corresponding to Ni^{3+} which is usually ignored because of its low intensity when compared with that of the Ni^{2+} satellite, but located ca. 5 eV upwards and consequently well resolved when a curve deconvolution process is carried out. The detection of the Ni^{3+} satellite may become crucial in the presence of other overlapping primary peaks (nickel aluminate/Ni^{3+}) for accurate interpretation of the XPS data.

Samples 2, 3, 6 and 8 (Table 3 and Fig. 5) with increasing nickel contents, calcined at 623 K, show the presence of the Ni $2p_{3/2}$ primary peak and the satellite peak of nickel aluminate at ca. 857 eV and 863 eV, respectively, also present in the reduced (673 K) samples 2r, 3r, 6r and 8r, indicating its unreducible nature at that temperature (Table 3 and Fig. 6). The hydroxyl groups of untreated γ-alumina should be responsible for the high interaction metal–support giving rise to the surface aluminate formation at a low temperature of 623 K. In this context, nickel aluminate from calcinations at 623–673 K was reported in the literature [25]. These E_b values characteristic of nickel aluminate are also in good agreement with others previously published [19,26]. Also, samples 2, 3, 6 and 8 show the presence of stoichiometric NiO at binding energies of the primary peaks of ca. 855.5 eV slightly higher than the 855.0 eV characteristic of the pure NiO value (sample 9), probably indicative of a weak interaction with the support. The reduced samples 2r, 3r, 6r and 8r show increasing content of reduced nickel at ca. 852.7 eV paralleling the increasing nickel contents of these samples. It is also worth remarking the absence of either stoichiometric or non-stoichiometric NiO in the reduced 2r, 3r, 6r and 8r samples showing the reduced nickel at E_b of ca. 853 eV and the primary peak and satellite of the unreducible (at 673 K) nickel aluminate (Fig. 6).

Fig. 7 shows the samples with increasing nickel content 10, 11, 12 and 13, 14, 15 calcined at 773 K and 1023 K, respectively. The non-resolved primary peaks at ca. 857 eV characteristic either of Ni^{3+} from non-stoichiometric NiO or the nickel aluminate may nevertheless be correctly assigned from the presence/absence of the Ni^{3+} satellite at ca. 867 eV. Then, the primary peaks exhibited at ca. 857 eV by samples 10, 11 and 13 from Fig. 7 together with all the reduced samples (at 673 K) of Fig. 8, which do not show the presence of the Ni^{3+} satellite, are assigned to the aluminate species. Samples 12, 14 and 15 with more nickel contents exhibit the presence of nickel aluminate and Ni^{3+} species this being lower for sample 15 calcined at a higher temperatures (Ni^{3+} is more reactive than Ni^{2+} towards the formation of aluminate). The two primary peaks of samples 10–15 (Table 3 and Fig. 7) at ca. 855 and 857 eV are assigned to stoichiometric NiO and nickel aluminate, respectively. Samples 13 (Fig. 7) and 13r (Fig. 8) of characteristic blue colours are considered as quite pure nickel aluminate with the primary peaks and satellites at ca. 857 and 863 eV, respectively. However, a small shift towards lower E_b values may be detected for the satellite when stoichiometric NiO is present at ca. 862.6 eV (Fig. 7).

The surface species detected so far in Figs. 5–7 (samples calcined up to 1023 K or calcined at 623 K followed by reduction at 673 K) are metallic nickel, stoichiometric and non-stoichiometric NiO and nickel aluminate. However, when calcinations are carried out at tempera-

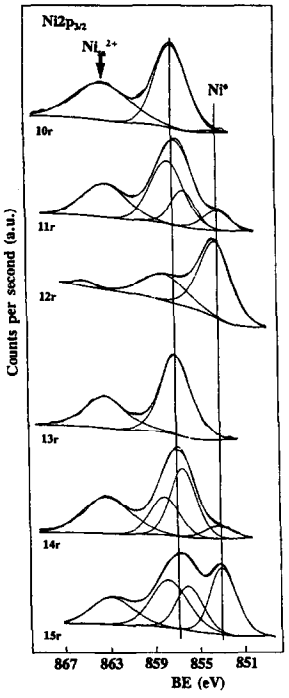

Fig. 8. XPS nickel/γ-alumina (samples 10r–12r and 13r–15r reduced at 673 K, previously calcined at 773 and 1023 K, respectively) for the Ni $2p_{3/2}$ level.

tures $\geqslant$ 773 K followed by reduction at 673 K significant changes may be brought about (Fig. 8). Samples 10r and 13r with the lower nickel contents show nickel aluminate mainly (with a very small amount of metallic nickel in sample 10r) where all the nickel is converted into nickel aluminate. Other peaks appear as nickel content increases; namely metallic nickel at ca. 853 eV and two more peaks are obtained from the curve deconvolution of samples 11r, 14r and 15r on the left and right sides of the aluminate E_b value, at ca. 858 and 856 eV (Fig. 8). The latter peak at 856 eV seems sufficiently shifted downwards to the right to obtain good resolving deconvolution with respect to the aluminate peak. This species is not present in the unreduced forms (Fig. 7) but shows up in the reduced samples 11r, 14r and 15r (Fig. 8). This species at ca. 856 eV may be assigned to a partially reduced non-stoichiometric aluminate shell obtained from the encapsulation of NiO in a shell of stoichiometry of the type of $NiO \cdot x(Al_2O_3)$, where $0 \leqslant x \leqslant 1$. A deeper characterization of the surface shell (the inner encapsulated NiO) seems less accessible to the XPS technique. In this content, similar results were reported in the literature regarding the partial reduction of the spinel $NiAl_2O_4$ at temperatures $>$ 723 K [27], the decoration of nickel crystallites by nickel aluminate [28–30], and the assumption of nickel particles being not tightly encapsulated but exhibiting voids and pores which guarantees the access of hydrogen through the aluminate shell [31–33]. The partial reduction of thin voided shells of a non-stoichiometric aluminate may begin at temperatures as low as 673 K, which must be responsible for the shift of E_b downwards at ca. 856 eV. In this case, the other primary peak shifted upwards at ca. 858 eV may be assigned to pure nickel aluminate, not purely detected so far unless a deconvolution curve is performed. The satellites of both peaks are not sufficiently far between themselves to allow deconvolution.

The XPS surface atomic intensities ratios Ni/Al together with the surface/chemical ratios are also depicted in Table 3. The surface atomic ratio generally increases with nickel content for any oxidic or reduced set of samples, the ratio for the reduced samples always being lower when compared with the same set of oxidic samples as expected from the smaller surface area of exposed metallic nickel. However, the quotient of surface(XPS)/chemical Ni/Al ratios (the chemical ratio being the Ni/Al atomic ratio derived from Table 1) should give us additional information of the nickel migration to the surface. Then, for the set of samples calcined at 623 K, the oxidized sample 2 with a surface/chemical value of 2.31 shows a relatively high surface nickel concentration with respect to the bulk concentration which is consistent with a highly surface dispersed NiO-rich non-stoichiometric nickel aluminate present on the surface. Sample 3, with a lower surface/chemical value of 1.72 may result from a partial surface encapsulation of NiO by the

non-stoichiometric aluminate shell which lowers the amount of nickel detectable by XPS. Sample 6, with more nickel content and a surface/chemical value of 2.72, may be indicative of the appearance of NiO crystallites on top of the surface, and the lowering of the value for sample 8 should be a consequence of the increase of the NiO crystallite sizes paralleling the increase of nickel content. A similar discussion may be followed for the other sets of samples except for the fact that at higher calcination temperatures the XPS aluminum intensities may increase with the more efficient formation of the stoichiometric aluminate phase, except in those cases, samples 12 and 15, of a relatively abundant NiO crystallite formation, as seen in Fig. 7. The reduced sets 2r–8r, 10r–12r and 13r–15r show parallel trends to the oxidic forms at lower values due to the smaller surface area exposed by metallic nickel when compared with NiO and nickel aluminate.

In summary, we envision the following picture of the system. A thin layer of nickel aluminate between zero and a few atoms thick, depending on calcination temperature and nickel concentration, covers the surface of the support. Catalytically active reduced nickel (for nitrile hydrogenations) either as naked crystallites or as encapsulated nickel inside voided non-stoichiometric aluminate shells lie on top of the underlying catalytically inactive nickel aluminate when precursor calcination temperatures are higher than 623 K and reduction temperatures of 673 K.

4. Conclusions

A structural characterization study of the system NiO/γ-alumina was carried out by means of surface area and porosimetry determinations of the solids. NiO crystallites are larger than the pore mouths of the support and little changes of the surface characteristics of the latter take place. Pore distributions lie in the mesopore region with diameters between 20 and 100 Å.

Powder XRD detects the oxidized and reduced-nickel phases present and does not detect the nickel aluminate phase, presumably because of the lack of crystallinity of the latter.

SEM micrographs detect the presence of octahedral NiO crystallites for heavier nickel loadings and amorphous nickel aluminate shelling NiO octahedra for mid nickel loadings.

The XPS results show the presence of surface Ni^{2+} (in the form of stoichiometric and non-stoichiometric NiO, and stoichiometric and non-stoichiometric nickel aluminates) and surface reduced nickel. A deconvolution of the experimental curves was carried out in order to obtain a better assignment of the surface nickel species present. Nickel aluminate is detected at calcination temperatures > 623 K and covers all the surface of the support with layers between zero and several atoms thick, depending on calcination temperature and nickel concentration. Catalytically active reduced nickel (for nitrile hydrogenations) either as naked crystallites or as encapsulated nickel inside voided non-stoichiometric aluminate shells lie on top of the underlying catalytically inactive nickel aluminate when precursor calcination temperatures are higher than 623 K with reduction temperatures of 673 K.

References

[1] P.N. Rylander, Catalytic Hydrogenation in Organic Syntheses, Academic Press, New York, 1979, pp. 138–140.
[2] German Pat. 3 402734 A1 (1984) to G. Frank and G. Neubauer, BASF, AG.
[3] F. Medina, P. Salagre, J.L.G. Fierro and J.E. Sueiras, J. Mol. Catal. A, 81 (1990) 363.
[4] F. Medina, P. Salagre, J.L.G. Fierro and J.E. Sueiras, Appl. Catal. A, 99 (1993) 115.
[5] F. Medina, P. Salagre, J.L.G. Fierro and J.E. Sueiras, J. Catal., 142 (1993) 392.
[6] F. Medina, P. Salagre, J.L.G. Fierro and J.E. Sueiras, J. Mol. Catal., 81 (1993) 387.
[7] J. Volf and J. Pasek, Stud. Surf. Sci. Catal., 27 (1983) 105.
[8] F. Medina, P. Salagre, J.L.G. Fierro and J.E. Sueiras, J. Chem. Soc., Faraday Trans., 90(10) (1994) 1455.
[9] M.J.F.M. Verhaak, Doctoral Thesis, Utrecht University, 1992.
[10] M. Lo Jacono, M. Schiarello and A. Cimino, J. Phys. Chem., 75 (1972) 1044.

[11] J.R.H. Ross, M.C.F. Steel and A. Zemi-Isfahani, J. Catal., 52 (1978) 280.
[12] M. Houalla and B. Delmon, J. Phys. Chem., 84 (1980) 2194.
[13] C.H. Bartholomew and W.L. Sorensen, J. Catal., 81 (1983) 131.
[14] A.M. Rubinstein, V.A. Akimov and L.D. Kretalova, Izv. Akad. Nauk SSSR, Otd. Khim. Nauk, (1958) 929.
[15] J.C. Vedrine, G. Hollinger and O.T. Minh, J. Phys. Chem., 82 (1978) 1515.
[16] M. Wu and D.M. Hercules, J. Phys. Chem., 83 (1979) 2003.
[17] R.B. Shalvoy, P.J. Reucroft and B.H. Davis, J. Vac. Sci. Technol., 17 (1980) 209.
[18] L.E. Alzamora, J.R.H. Ross, E.C. Kruissink and L.L. Van Reijen, J. Chem. Soc., Faraday Trans., 77 (1981) 665.
[19] G.R. Gavalas, C. Phichitkul and G.E. Voecks, J. Catal., 88 (1984) 54.
[20] J. Zielinsky, J. Catal., 76 (1982) 157.
[21] O. Solcova, K. Jiratova, D.C. Ueiker and U. Steinike, Appl. Catal., 94 (1993) 153.
[22] E.P. Barrett, L.G. Joyner and P.P. Halenda, J. Am. Chem. Soc., 73 (1951) 373.
[23] S. Brunauer, L.S. Deming, W.S. Deming and E. Teller, J. Am. Chem. Soc., 62 (1940) 1723.
[24] J.H. de Boer, in D.H. Everett and F. Stone (Eds.), The Structure and Properties of Porous Materials, Butterworths, London, 1958, p. 68.
[25] K. Ahmed and P. Mistry, Collect. Czech. Chem. Commun., 57 (10) (1992) 2073.
[26] S. Narayanan and K. Uma, J. Chem. Soc., Faraday Trans., 81 (1985) 2733.
[27] I.A.P.S. Murthy and C.S. Swamy, J. Mater. Sci., 28 (1993) 1194.
[28] R. Lamber and G. Schulz-Ekloff, Surf. Sci., 258 (1991) 107.
[29] L. Kubelková, J. Nováková, N.I. Jaeger and G. Schulz-Ekloff, Appl. Catal. A: Gen., 95 (1993) 87.
[30] J. Zielinski, Appl. Catal., 94 (1993) 107.
[31] Y.J. Huang, J.A. Schwarz, J.R. Diehl and J.P. Baltrus, Appl. Catal., 37 (1988) 229.
[32] R. Lamber and G. Schulz-Ekloff, J. Catal., 146 (1994) 601.
[33] F. Medina, P. Salagre, J.L.G. Fierro and J.E. Sueiras, J. Chem. Soc., Faraday Trans., 89(18) (1993) 3507.